RSC Advances

ROYAL SOCIETY OF CHEMISTRY

www.rsc.org/advances

Table of contents entry

* Colour graphic: maximum size 8 cm x 4 cm

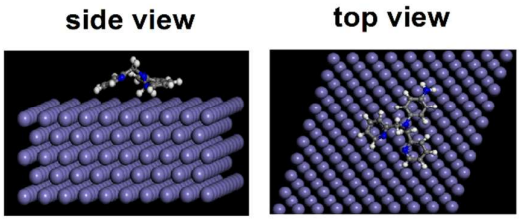

* Text: one sentence, of maximum 20 words, highlighting the novelty of the work.

evaluate the inhibition properties of a pyridine derivative with more than one pyridine ring, 4-amino-N,N-di-(2-pyridylmethyl)-aniline, on mild steel in HCl

RSC Advances

RSCPublishing

ARTICLE

Experimental and theoretical studies on the corrosion inhibition performance of 4-amino-N, N-di-(2-pyridylmethyl)-aniline on mild steel in hydrochloric acid†

Cite this: DOI: 10.1039/x0xx00000x

Received 00th May 2015,
Accepted 00th May 2015

DOI: 10.1039/x0xx00000x

www.rsc.org/

Bin Xu,[a] Yan Ji,[a] Xueqiong Zhang,[a] Xiaodong Jin,[a] Wenzhong Yang,[a]* and Yizhong Chen[b]

The corrosion inhibition properties of a pyridine derivative with more than one pyridine ring, 4-amino-N, N-di-(2-pyridylmethyl)-aniline, on mild steel in 1.0 M hydrochloric acid were estimated by potentiodynamic polarization, electrochemical impedance spectroscopy and surface analysis methods. The results showed that 4-amino-N, N-di-(2-pyridylmethyl)-aniline was a mixed type inhibitor and the inhibition efficiency decreased with the rise in temperature. The adsorption process followed the Langmuir adsorption isotherm. The thermodynamic parameters responsible for the adsorption process were also discussed. Quantum chemical calculations were performed to correlate electronic structure parameters of 4-amino-N, N-di-(2-pyridylmethyl)-aniline with its inhibition performance. Molecular dynamics simulations were also used to investigate the equilibrium configurations of 4-amino-N, N-di-(2-pyridylmethyl)-aniline on the iron surface.

1. Introduction

Mild steel is considered as one of the most important construction and engineering materials because its price is relatively low while it provides material properties that are acceptable for many applications. Generally, hydrochloric acid is widely employed in industrial processes, such as acid cleaning, acid descaling and oil well acidification.[1-3] Unfortunately, the corrosion of mild steel in the aggressive acid solution leads to huge economic losses. Among the corrosion prevention techniques, the use of inhibitors is the most efficient and practical method to overcome corrosion.[4] It is well known that heterocyclic organic compounds, containing heteroatoms, electronegative functional groups and π electrons, are often found to work as efficient corrosion inhibitors.[5-7] Meanwhile, the adsorption characteristics which determine the inhibition performance of compounds are often affected by the molecular size, functional groups, the electron density at the donor atoms, etc..[8, 9]

In recent years, many researchers have oriented their interest to the corrosion inhibition behavior of pyridine derivatives, including 2-amino-3,5-dicarbonitrile-4-(4-methoxyphenyl)-6-(phenylthio) pyridine,[10] 2-amino-3,5-dicarbonitrile-4-phenyl-6-(phenylthio) pyridine,[10] 2-amino-3,5-dicarbonitrile-4-(4-nitrophenyl)-6-(phenylthio) pyridine,[10] 2-amino-5-(3-pyridyl)-1,3,4-thiadiazole,[11] 2-amino-5-(4-pyridyl)-1,3,4-thiadiazole,[11] pyridine-2-thiol,[12] 2-pyridyl disulfide,[12] 2-pyridinecarbonitrile,[13] 2-amino-4-methylpyridine,[14] and 2-(4-pyridyl)-benzimidazole.[15] The presence of nitrogen atom and electron rich structure can facilitate the adsorption of pyridine derivatives onto metal surface. However, a perusal of literature[10-15] reveals that the most studied pyridine derivatives contain only one pyridine ring and the studies on the pyridine derivatives with two or more pyridine rings are still scarce. In the current study, the studied inhibitor, 4-amino-N, N-di-(2-pyridylmethyl)-aniline (APMA), contains two pyridine rings and an aniline ring. Recently, theoretical calculation methods have been widely used to investigate the mechanism of corrosion.[16] Quantum chemical calculations have been proved to be a useful tool for studying the correlation of the electronic properties and the corrosion inhibition efficiency.[17, 18] In addition, the molecular dynamics simulations can provide insights into the configuration and adsorption energy of inhibitor molecules adsorbed on the metal surface at a molecular level.[19, 20]

Consequently, the aim of the present work is to evaluate the corrosion inhibition effectiveness of APMA on mild steel in 1.0 M hydrochloric acid by utilizing electrochemical techniques, surface analysis and theoretical calculation methods. Besides,

an attempt is made to elucidate the corrosion inhibition mechanism.

2. Experimental Section

2.1. Materials

The mild steel performed in this study possesses the following chemical composition (wt. %): 0.37 % Mn, 0.17 % C, 0.20 % Si, 0.03 % S, 0.01 % P and remainder Fe. The mild steel disk used for electrochemical measurements was mounted in epoxy resin with an area of 0.785 cm^2 exposed to the electrolyte. Prior to the experiments, the mild steel disk was abraded with different emery papers (grades 500, 1000, 1500 and 2000), rinsed with double distilled water, degreased in ethanol, and finally dried at room temperature. The acid solution (1.0 M HCl) was prepared by dilution of analytical grade 37% hydrochloric acid with double distilled water. The concentration range of APMA employed was varied from 0.5 mM to 2.0 mM.

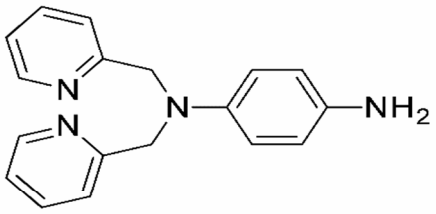

Fig. 1 Chemical structure of APMA

The studied inhibitor, APMA, shown in Fig. 1 was synthesized as reported earlier.[21] A solution of di-tert-butyldicarbonate (0.046 mol) in 1, 4-dioxane was added dropwise to a solution of p-phenylenediamine. Triethylamine (0.046 mol) was then added to the reaction mixture, and the solution was heated at 60 °C for 24 h. Solvent was removed in vacuo to yield a brown oil. Crude product was purified via flash column chromatography (ethyl acetate/petroleum ether=3:1) to give the desired product, (4-aminophenyl) carbamic acid tert-butyl ester. To a solution of it (0.019 mol) in anhydrous ethanol was added Na_2CO_3 (0.077 mol). 2-(Chloromethyl)-pyridine hydrochloride (0.038 mol) was then added, and the mixture was heated to reflux at 80 °C for 24 h. The resulting brown suspension was filtered, and the solvent was removed in vacuo to yield a brown oil. The brown oil was diluted with CH_2Cl_2 and treated with 2 M NaOH. Product was extracted with CH_2Cl_2, then the organic layer was washed with brine and dried over Na_2SO_4, and the CH_2Cl_2 was removed under vacuum. The crude product was run through a silica plug to give the desired product as an orange solid. The orange solid (2.56 mmol) was dissolved in ethyl acetate and then treated dropwise with 12 M HCl. The reaction mixture was left to stir for 1 h. The resultant solution was combined with 5 M NaOH, and the organic layer was extracted with CH_2Cl_2. Solvent was removed in vacuo to yield the APMA. Identification of the structure of the synthesized APMA was performed by ^{1}H NMR, ^{13}C NMR, MS and FTIR. (see ESI†, Fig. S1-S4) ^{1}H NMR (500 MH_Z, DMSO-d_6): δ 4.32 (s, 2 H), 4.62 (s, 4 H), 6.40 (d, J = 7.75 H_Z, 2 H), 6.47 (d, J = 7.85 H_Z, 2 H), 7.19 (m, 2 H), 7.27 (d, J = 7.7 H_Z, 2 H), 7.67 (m, J = 14.6 H_Z, 2 H), 8.49 (d, J = 3.25 H_Z, 2 H). ^{13}C NMR (500 MH_Z, DMSO-d_6): δ 159.68, 148.95, 139.74, 139.60, 136.38, 121.78, 121.23, 115.22, 114.73, 57.89. MS (ESI) m/z (%) 313.1 (100) M^++Na. IR ν (KBr, cm^{-1}) 3401, 3303, 3204, 3012, 1621, 1589, 1517, 1470, 1433, 1388, 1353, 813, 762.

2.2. Electrochemical measurements

All the electrochemical measurements were conducted using ZAHNER IM6ex electrochemical workstation, controlled by ZAHNER THALES software. A traditional three-electrode cell assembly was carried out in all electrochemical measurements. The mild steel disk was used as the working electrode and a platinum plate with a surface area of 1.0 cm^2 was served as the auxiliary electrode, respectively. A saturated calomel electrode (SCE) coupled to a fine Luggin capillary was used as the reference electrode. The Luggin capillary was kept close to the working electrode to decrease IR drop. All the electrochemical measurements were carried out in non-deaerated solution under unstirred condition at constant temperature controlled by a thermostatic water bath. Before the electrochemical measurements, the working electrode was immersed in the test solution for 30 min to reach a steady-state potential. The potentiodynamic polarization curves were recorded in the potential range - 700 to - 300 mV (vs. SCE) with a scan rate of 0.001 V s^{-1}. Electrochemical impedance spectroscopy (EIS) were carried out in a frequency range from 10^{-1} - 10^5 Hz with a 5 mV peak-to-peak voltage excitation at open circuit potential.

2.3. SEM-EDX studies

The morphologies of specimens after immersed in 1.0 M HCl with and without 2.0 mM APMA for a duration of 12 h at 30 °C were analyzed by using scanning electron microscopy (JEOL JSM-6510) at high vacuum. Chemical composition of the specimens was recorded by an EDX detector (NORAN VANTAGE DSI) coupled to the SEM.

2.4. X-ray photoelectron spectroscopy (XPS)

XPS experiments were carried out by a PHI 5000 VersaProbe spectrometer with the monochromatized Al Kα X-ray source ($h\nu$ = 1486.4 eV) and an X-ray beam of around 100 μm. The analyser was operated in constant pass energy of 58.7 eV using an analysis area of 1 cm × 1 cm. The binding energy scale was initially calibrated using Ag $3d_{5/2}$ (368.2 eV) level and pressure was in the range of 6.7 × 10^{-10} mbar during the experiments. Then XPS Peak software was employed to fit the experimental curve. The analyses were practiced on the mild steel specimen immersed in 1.0 M HCl with 2.0 mM APMA for 12 h at 30 °C. The specimen was pre-treated by the same procedure described in Section 2.1.

2.5. Quantum chemical calculations

Quantum chemical calculations were conducted with DMol ^{3} module in Materials Studio software 7.0. All electron calculations were performed with the generalized gradient approximation (GGA) functional of BLYP in conjunction with double zeta plus polarization (DNP) double-numeric basis set.[22, 23] BLYP derived from the combination of Becke for the exchange part and Lee, Yang and Parr for the correlation part is a popular function.[24] The DNP basis sets are of comparable quality to 6-31G Gaussian basis sets.[25] Fine convergence

accuracy and global orbital cutoffs were employed on basis set definitions. Frequency analysis was performed to ensure that the calculated structure is the minimum point on potential energy surface (without imaginary frequency).

2.6. Molecular dynamics simulations

Molecular dynamics (MD) simulations were performed using the Discover module in Material Studio 7.0 to model the adsorption process of inhibitor molecules onto Fe (1 1 0) surface. The MD simulations were conducted in a three-dimensional simulation box (22.34 Å × 22.34 Å × 38.11 Å) with periodic boundary conditions to model a representative part of the interface without any arbitrary boundary effects. The Fe (1 1 0) surface was first built and relaxed by minimizing its energy according to molecular mechanics, then the surface area was enlarged by constructing an appropriate super cell. After that, vacuum slab with 30 Å thickness was built on the Fe (1 1 0) surface and the system was optimized using COMPASS (condensed-phase optimized molecular potentials for atomistic simulation studies) force field.[11, 15, 18, 22] During the simulations, the Fe slab was kept "frozen", and the inhibitor molecule was allowed to reach the Fe surface freely. MD simulations were performed at 303 K, NVT (dynamics at fixed volume with a thermostat to maintain a constant temperature) ensemble, with a time step of 1.0 fs and simulation time of 100 ps. The trajectory was recorded every 5000 fs. The interaction energy (E_{int}) between the inhibitor molecule and the Fe (1 1 0) surface was calculated as follows:

$$E_{int} = E_{total} - (E_{surface} + E_{inh}) \quad (1)$$

where E_{total} is the total energy of the simulation system, $E_{surface}$ and E_{inh} are the energies of iron crystal and free inhibitor molecule, respectively. The binding energy (E_{bin}) is the negative value of the interaction energy[17, 19, 22]

$$E_{bin} = - E_{int} \quad (2)$$

3. Results and discussion

3.1. Open circuit potential measurements

The variation of open circuit potential (E_{ocp}) of working electrode with time in 1.0 M HCl in the absence and presence of APMA at 30 °C is graphically represented in Fig. 2. Apparently, E_{ocp} moved to more positive value with time and gradually remained unchanged, which was similar to the previously reported articles.[23, 26] It took about 1500 s to reach the steady-state, so the working electrode was immersed into the test solution for 30 min before each electrochemical measurement.

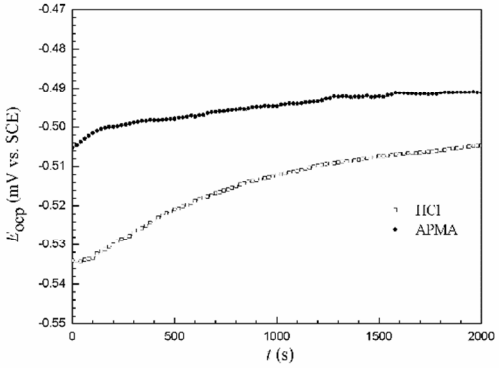

Fig. 2 E_{ocp} - t curves for mild steel in 1.0 M HCl in the absence and presence of APMA at 30 °C

3.2. Potentiodynamic polarization measurements

The information about the kinetics of corrosion reactions can be provided by the potentiodynamic polarization measurements.[27, 28] Fig. 3 represents the potentiodynamic polarization curves for mild steel immersed in 1.0 M HCl at 30 °C in the absence and presence of APMA.

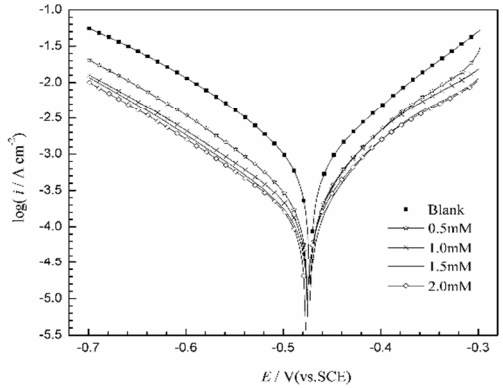

Fig. 3. Potentiodynamic polarization curves for mild steel in 1.0 M HCl in the absence and presence of different concentrations of APMA at 30 °C

From Fig. 3, it is clear that both anodic and cathodic Tafel curves shift towards the lower current densities in the presence of APMA. This phenomenon implies that both anodic metal dissolution and cathodic hydrogen evolution reactions are retarded. Meanwhile, this suppression effect becomes more pronounced with the increasing APMA concentration. The electrochemical parameters such as corrosion potential (E_{corr}), corrosion current density (i_{corr}), anodic Tafel slope (b_a) and cathodic Tafel slope (b_c), obtained by extrapolating the anodic and cathodic Tafel curves to the point of intersection, are summarized in Table 1. The corrosion inhibition efficiency (η_p) calculated by the following equation is also listed in Table 1.

$$\eta_p = (1 - i_{corr} / i_{corr0}) \times 100\% \quad (3)$$

where i_{corr0} and i_{corr} represent the corrosion current densities of mild steel in the absence and presence of APMA, respectively. According to the literature, [29-31] it has been reported that if the displacement in E_{corr} in the presence of inhibitor is more than 85 mV with respect to E_{corr} of the blank, the inhibitor can be recognized as cathodic or anodic type. On the contrary, if the displacement in E_{corr} is less than 85 mV, the inhibitor can be classified as a mixed type. In the present study, the maximum shift is 20.5 mV and the E_{corr} shifts towards negative side in the presence of APMA, which indicates that APMA acts as a mixed type inhibitor and has more influence on the cathodic polarization plots. Inspection of Table 1 reveals that the corrosion current density decreases significantly in the presence of APMA, and η_p increases sharply with the increase in the concentration of APMA. Furthermore, the values of b_c and b_a exhibit no obvious changes, which suggests that the inhibition effect comes from the reduction of the reaction area on the corroding metal surface.[23] Namely, the corrosion inhibition is caused by geometric blocking of the active reaction sites on the metal surface without modifying the corrosion mechanism of mild steel in hydrochloric acid.[32, 33]

RSC Advances

RSCPublishing

ARTICLE

Table 1 Potentiodynamic polarization parameters for mild steel in 1.0 M HCl in the absence and presence of different concentrations of APMA at 30 °C

C (mM)	E_{corr} (mV vs.SCE)	I_{corr} (mA cm^{-2})	$-b_c$ (mV dec^{-1})	b_a (mV dec^{-1})	η_p (%)	θ_p
Blank	-467.1 ± 6.4	0.783 ± 0.092	113 ± 8	87.4 ± 0.8	-	-
0.5	-475.8 ± 0.6	0.303 ± 0.027	117 ± 5	88.8 ± 2.9	61.3	0.613
1.0	-487.6 ± 5.1	0.225 ± 0.011	115 ± 3	90.8 ± 3.1	71.3	0.713
1.5	-485.4 ± 4.2	0.187 ± 0.020	115 ± 3	93.4 ± 2.8	76.1	0.761
2.0	-481.9 ± 2.1	0.149 ± 0.026	114 ± 7	80.1 ± 6.1	81.0	0.810

3.3. Electrochemical impedance spectroscopy

Electrochemical impedance spectroscopy (EIS) is a valuable tool to evaluate the protective properties of inhibitors on metal surface.[17] Fig. 4 presents the Nyquist plots for mild steel in 1.0 M HCl at 30 °C in the absence and presence of APMA. All the impedance spectra displayed in Fig. 4 reveal a single depressed capacitive semicircle across the studied frequency range, which denotes that the dissolution process is related to the charge transfer process.[10, 34] Noticeably, these impedance loops are not perfect semicircles, which can be termed as frequency dispersion effect as a result of the roughness and inhomogeneity of the metal electrode surface.[35, 36] Furthermore, the diameters of the capacitive loops increase sharply with the increasing concentration of APMA and the shape of the loops doesn't modify. The Bode plots recorded for mild steel immersed in 1.0 M HCl with and without APMA are shown in Fig. 5. It is clear that only one phase peak at the middle frequency range can be observed, confirming that there is only one time constant. Meanwhile, the increasing concentration of APMA conduces to the increase in the impedance modulus at low frequency and the more negative values of phase angle at intermediate frequency, demonstrating the adsorption of APMA onto mild steel surface.[17]

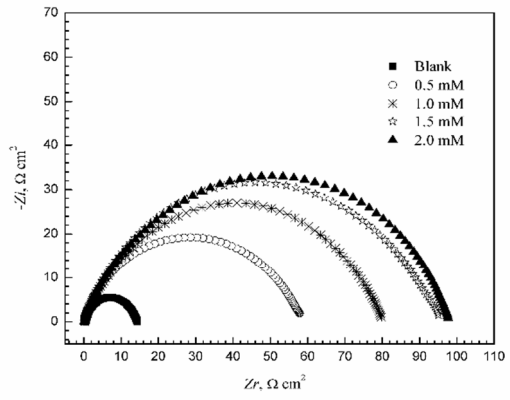

Fig. 4. Nyquist plots for mild steel in 1.0 M HCl in the absence and presence of different concentrations of APMA at 30 ºC

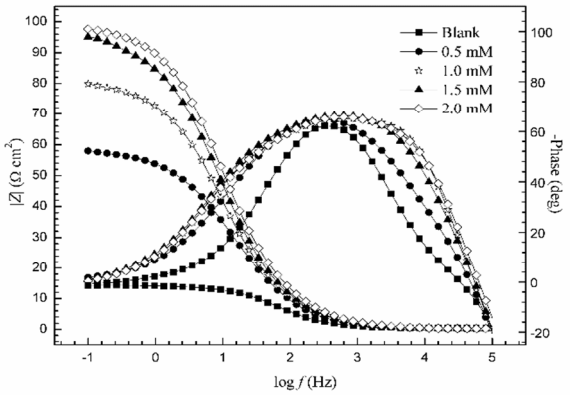

Fig. 5. Bode plots for mild steel in 1.0 M HCl solution in the absence and presence of different concentrations of APMA at 30 ºC

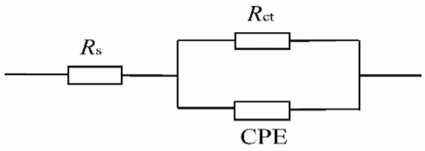

Fig. 6. Randle's equivalent circuit model used to fit the EIS data

According to the above results, The EIS data are analyzed via the Randle's equivalent circuit (Fig. 6) that includes the solution resistance (R_s), polarization resistance (R_p) and constant phase element (CPE), which can be represented as follows: [22, 37]

$$Z_{CPE} = Y_0^{-1}(j\omega)^{-n} \quad (4)$$

where Y_0 is the CPE constant, n is the phase shift, j is the imaginary unit and ω is the angular frequency. Thus the values of the double

layer capacitance (C_{dl}) and inhibition efficiency (η_e) are calculated according to the following equations:

$$C_{dl} = Y_0(\omega_m)^{n-1} \quad (5)$$

$$\eta_e = (1 - R_{p0} / R_p) \times 100\% \quad (6)$$

where ω_m represents the angular frequency at the maximum value of the imaginary part. R_{p0} and R_p stand for the polarization resistance in the absence and presence of APMA, respectively. The representative example of using the equivalent circuit to fit the experimental data for mild steel in 1.0 M HCl with 2.0 mM APMA is shown in Fig. 7 and the electrochemical parameters are listed in Table 2.

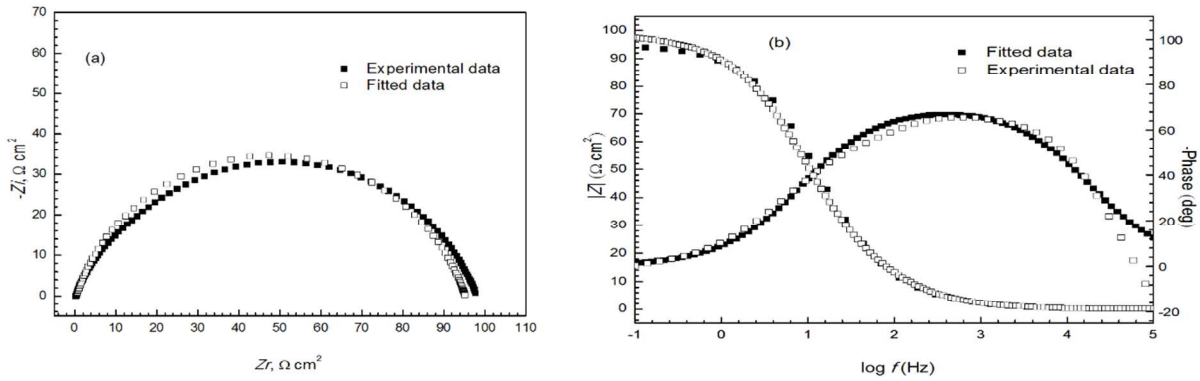

Fig. 7. The representative figure of using the equivalent circuit to fit the experimental data of EIS for mild steel in 1.0 M HCl with 2.0 mM APMA

(a) Nyquist plot (b) Bode plot

It can be seen that R_s is small, which supports that the IR drop can be negligible.[23] It is apparent that the value of R_p increases significantly with the increasing APMA concentration while the value of C_{dl} decreases. The larger R_p and the smaller C_{dl} are related to an increase in the surface coverage by APMA molecules, resulting in an increase in inhibition efficiency. The maximum η_e reaches up to 85.7 % at 2.0 mM. According to Helmholtz model:

$$C_{dl} = \varepsilon^0 \varepsilon A / d \quad (7)$$

where ε is the local dielectric constant, ε^0 is the free space permittivity, d is the thickness of the interfacial layer and A is the electrode area. The decrease in C_{dl} is due to a decrease in the local dielectric constant or an increase in the thickness of the electrical double layer, which in turn justify that APMA reduces the metal dissolution by effective adsorption. Therefore, it is suggested that APMA molecules adsorb at metal/solution interface by replacing water molecules. It is worth noting that the inhibition efficiencies calculated from the EIS measurements show the same trend as that obtained from potentiodynamic polarization measurements.

Table 2 Impedance data for mild steel in 1.0 M HCl in absence and presence of different concentrations of APMA at 30 ℃

C (mM)	R_s (Ω cm ²)	R_p (Ω cm ²)	n	C_{dl} (μF cm ⁻²)	η_e (%)	θ_e
Blank	0.36 ± 0.03	13.6 ± 2.0	0.88 ± 0.02	269.4 ± 14.5	-	-
0.5	0.32 ± 0.08	55.9 ± 8.8	0.81 ± 0.03	250.3 ± 26.4	75.7	0.757
1.0	0.18 ± 0.04	76.7 ± 6.7	0.80 ± 0.04	240.0 ± 10.5	82.3	0.823
1.5	0.22 ± 0.06	90.7 ± 10.2	0.80 ± 0.05	226.1 ± 13.5	85.0	0.850
2.0	0.21 ± 0.05	95.0 ± 11.4	0.80 ± 0.02	199.6 ± 18.1	85.7	0.857

3.4. Adsorption isotherm

It is crucial to know the mode of adsorption as well as the adsorption isotherm which can provide basic information about the corrosion inhibition action between APMA molecules and the mild steel surface. The adsorption process of organic inhibitor molecules can be considered as a result of replacement of water molecules adsorbed on the metal surface according to the following process:

$$APMA_{(sol)} + n\ H_2O_{(ads)} \rightarrow APMA_{(ads)} + n\ H_2O_{(sol)} \quad (8)$$

where $APMA_{(sol)}$ and $APMA_{(ads)}$ represent the APMA molecules in the solution and adsorbed on the metal surface, respectively. n is the number of water molecules replaced by one organic molecule. In order to characterize the adsorption of APMA, various isotherms were employed to fit the experimental data, such as Langmuir, Temkin, Frumkin, Flory-Huggins and Freundlich adsorption isotherms. Thus the surface coverage (θ) is defined as:

$$\theta = \eta / 100 \quad (9)$$

In order to yield the best fit isotherm model, the values of η are obtained from potentiodynamic polarization and EIS measurements, respectively. According to the data, it can be concluded that the best description of the adsorption behavior of APMA can be explained by Langmuir adsorption isotherm:

$$C / \theta = 1 / K_{ads} + C \quad (10)$$

where C is the concentration of APMA, K_{ads} is the equilibrium constant for the adsorption-desorption process.

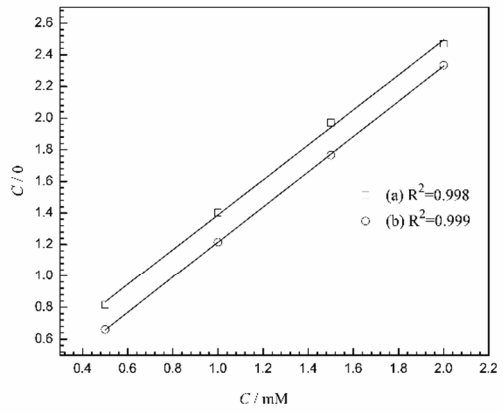

Fig. 8. Langmuir adsorption plots for mild steel in 1.0 M HCl with APMA at 30 °C. (a) potentiodynamic polarization data, (b) EIS data

The plots in Fig. 8 were found to be linear, with slopes of 1.106 (line a) and 1.114 (line b), respectively. The interactions between the APMA species on the metal surface and the changes in the adsorption heat conduce to the divergence of the slopes from unity.[37]

According to Langmuir adsorption isotherm, the value of K_{ads} can be obtained from the intercept of the straight line in Fig. 8 and K_{ads} is also related to the standard free energy of adsorption (ΔG^0) by the following equation:

$$\Delta G^0 = - RT \ln(55.5\ K_{ads}) \quad (11)$$

where T is the absolute temperature, R is the universal gas constant. The calculated values of K_{ads} and ΔG^0 are 3540 M^{-1}, - 30.7 kJ mol^{-1} (line a) and 9884 M^{-1}, - 33.3 kJ mol^{-1} (line b), respectively. The high negative ΔG^0 values ensure strong and spontaneous adsorption of APMA film on the mild steel surface.[11, 37]

3.5. Effect of temperature

To evaluate the effect of temperature on the inhibitive performance of APMA on mild steel surface in 1.0 M HCl, potentiodynamic polarization measurements were carried out in the temperature range of 30 - 50 °C in the absence and presence of 2.0 mM APMA, as shown in Fig. 9. The activation energy (E_a) of the corrosion process could be determined by the Arrhenius equation:[18, 19]

$$\ln i_{corr} = - E_a / RT + \ln A \quad (12)$$

where E_a is the apparent activation energy, A is the Arrhenius pre-exponential factor and T is the absolute temperature.

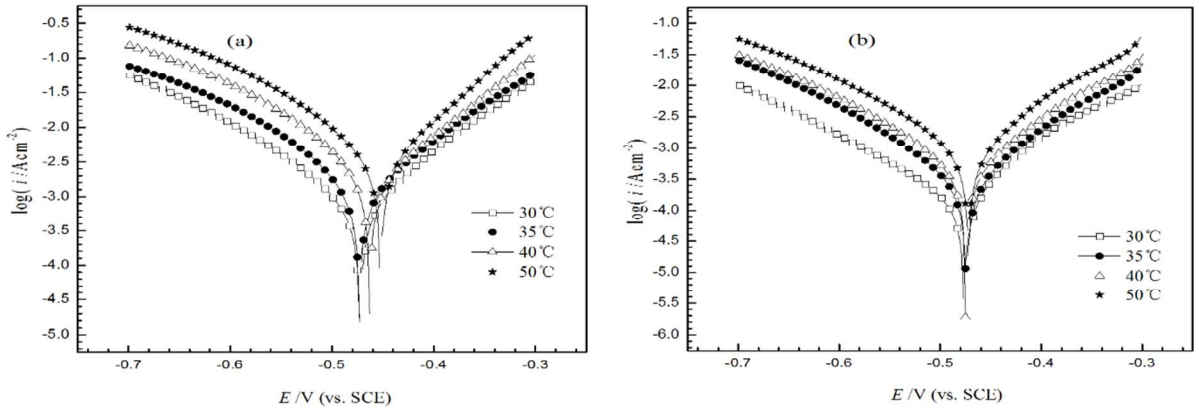

Fig. 9. Potentiodynamic polarization curves for mild steel in 1.0 M HCl in the absence and presence of 2.0 mM APMA at different temperatures: (a) blank, (b) APMA.

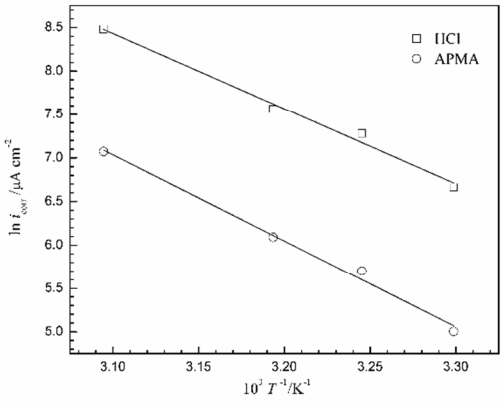

Fig. 10. Arrhenius plots for mild steel in 1.0 M HCl and 1.0 M HCl +2.0 mM APMA.

Fig. 10 represents the Arrhenius plots of ln i_{corr} versus $1/T$ for mild steel in 1.0 M HCl with and without APMA. The change in the enthalpy of activation (ΔH^*) and the entropy of activation (ΔS^*) can be calculated by using the transition state equation:

$$i_{corr} = \frac{RT}{Nh} \exp(-\frac{\Delta H^*}{RT}) \exp(\frac{\Delta S^*}{R}) \quad (13)$$

where h is the Planck's constant, N is Avogadro's number. The transition state plots of ln (i_{corr} / T) versus $1/T$ are depicted in Fig. 11.

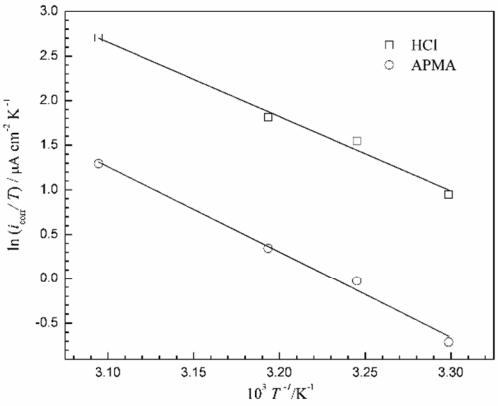

Fig. 11. Transition state plots for mild steel in 1.0 M HCl and 1.0 M HCl + 2.0 mM APMA

Corresponding electrochemical results and thermodynamic parameters are listed in Table 3. As seen from Fig. 10 and Table 3, the i_{corr} increases with the rise in temperature while the inhibition efficiency decreases, which may be due to the fact that higher temperature accelerates the desorption capacity of APMA on the mild steel surface.[29, 38] It is apparent that the value of E_a for the inhibited solution (82.2 kJ mol^{-1}) is higher than that for uninhibited solution (71.9 kJ mol^{-1}), indicating that the dissolution of metal is decreased by an energy barrier made by the adsorption of inhibitors.[4] The positive sign of ΔH^* reflects the endothermic nature of mild steel dissolution process and more energy barrier is required for the dissolution of metal in the presence of APMA.[29] The increase in the value of ΔS^* implies an increase in disordering takes place during the adsorption process on going from reactants to the activated complex.[39]

Table 3 Effect of temperature on electrochemical parameters of the corrosion in 1.0 M HCl in the absence and presence of 2.0 mM APMA

Inhibitor	*Temp.* (°C)	E_{corr} (mV vs.SCE)	I_{corr} (mA cm^{-2})	η_p (%)	ΔE_a (kJ mol^{-1})	ΔS_a (J mol^{-1} K^{-1})	ΔH_a (kJ mol^{-1})
Blank	30	-467.1 ± 6.4	0.783 ± 0.092	-	71.9	39.4	69.3
	35	-458.1 ± 5.8	1.452 ± 0.191	-			
	40	-452.5 ± 7.7	1.923 ± 0.127	-			
	50	-426.4 ± 9.7	4.828 ± 0.102	-			
APMA	30	-481.9 ± 2.1	0.149 ± 0.026	81.0	82.2	59.8	79.6
	35	-471.8 ± 2.7	0.299 ± 0.039	79.4			
	40	-466.1 ± 4.4	0.442 ± 0.034	77.0			
	50	-475.0 ± 2.2	1.180 ± 0.032	75.6			

3.6. Surface analysis

SEM micrographs and corresponding EDX spectra of mild steel specimens before and after immersed in 1.0 M HCl with and without APMA are shown in Fig. 12. Fig. 12a shows an SEM micrograph of the mild steel specimen before immersed in 1.0 M HCl and the abrading scratches can be clearly observed. The corresponding EDX analysis (Fig. 12b) shows that the Fe is the main element in addition to C. It can be clearly seen from Fig. 12c that the mild steel surface was seriously damaged in hydrochloric acid solution. However, in the presence of APMA, the damage of the mild steel was significantly reduced (Fig. 12e). A cleaner and smoother mild steel surface can be observed in comparison to that in the absence of APMA. The percentages of the elements (weight %) found on the mild steel surface in Fig. 12d and Fig. 12f are 11.26% O, 7.86% C, 80.87% Fe and 3.62% O, 9.96% C, 82.95% Fe, 3.47% N, respectively. Close examination of the corresponding EDX analysis reveals that the decrease in O and the presence of N on the inhibited mild steel surface, confirming the adsorption of APMA on the metal surface.

RSC Advances

RSCPublishing

ARTICLE

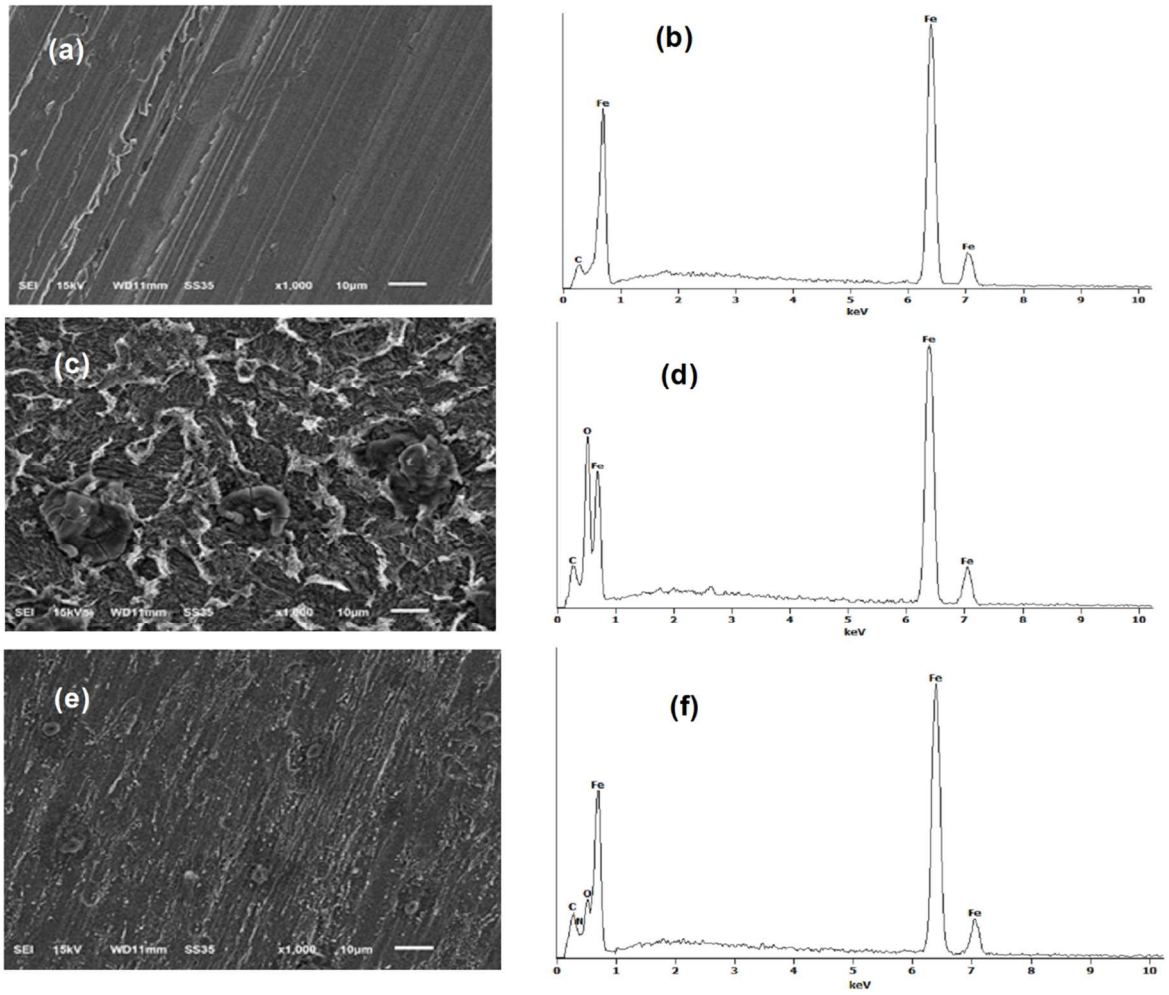

Fig. 12. SEM micrograph (a) and EDX analysis (b) of mild steel before immersed in HCl; SEM micrograph (c) and EDX analysis (d) of mild steel after immersed in 1.0 M HCl without APMA; SEM micrograph (e) and EDX analysis (f) of mild steel after immersed in 1.0 M HCl with APMA

It is well known that XPS is a powerful tool for probing the adsorption of inhibitors on metal surface.[40, 41] Thus we performed XPS experiments on the mild steel immersed in 1.0 M HCl with 2.0 mM APMA. High resolution XPS spectra of the protected mild steel are illustrated in Fig. 13. The C 1s spectrum is shown in Fig. 13a and is fitted to three peaks. The peaks of binding energy at 284.2 and 284.9 eV can be attributed to the C-C, C=C and C-H aromatic bonds in benzene ring and pyridine ring. The peak at 287.9 eV maybe assigned to the carbon atom bonded to nitrogen in CH_2-N. The deconvolution of the O 1s spectrum is fitted into two main peaks (Fig. 13b). The first peak (529.6 eV) is assigned to O^{2-}, and in principle could be related to oxygen atoms bonded to ferric oxides.[42] The second peak (531.1 eV) can be ascribed to OH^- of hydrous iron oxides, such as FeOOH and/or $Fe(OH)_3$.[43] The Fe 2p spectrum (Fig. 13c) depicts a double peak profile located at a binding energy around 711 eV (Fe $2p_{3/2}$) and 725 eV (Fe $2p_{1/2}$) together with an associated ghost structure.[43] Deconvolution of the high resolution Fe $2p_{3/2}$ XPS spectrum consists three peaks. The first peak located at 711.1 eV can be assigned to Fe^{3+} due to the presence of the Fe_2O_3 and/or FeOOH. The second peak at 714.0 eV is attributed to the presence of small concentration of $FeCl_3$ on the metal surface.[44] The last peak at 718.3 eV can be ascribed to the satellites of the ferric compounds. From these previous observations, the XPS results support the adsorption of APMA on the mild steel surface.

RSC Advances

RSCPublishing

ARTICLE

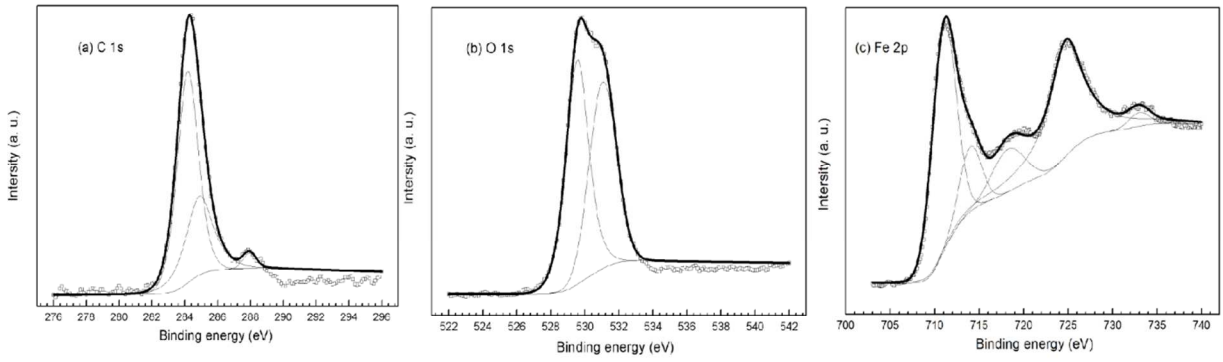

Fig. 13. High resolution XPS of C 1s(a), O 1s(b) and Fe 2p(c) for mild steel after immersed in 1.0 M HCl with 2.0 mM APMA

3.7. Quantum chemical calculations

The effectiveness of an inhibitor is influenced by its spatial molecular structure as well as its molecular electronic structure. In this regard, quantum chemical calculations were performed to investigate the structural and electronic properties of APMA. The optimized structure and the frontier molecular orbital density distributions of APMA are given in Fig. 14 and Fig. 15, respectively. All the quantum chemical parameters are listed in Table 4.

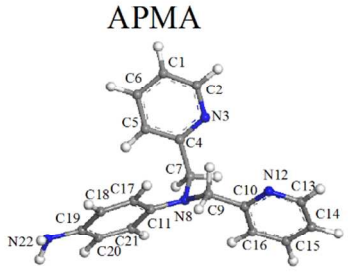

Fig. 14. The optimized structures of APMA

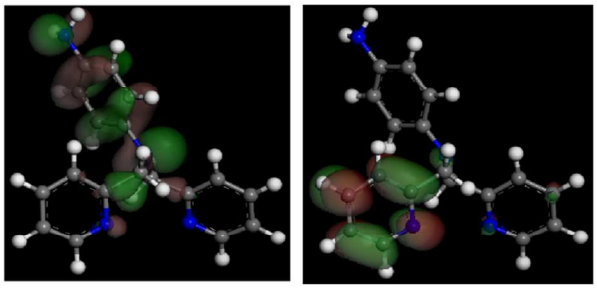

Fig. 15. Frontier molecular orbital density distributions of APMA

According to the frontier molecular orbital theory, the density distributions of HOMO and LUMO are very critical for the prediction of the reactivity of a chemical species. The E_{HOMO} (the highest occupied molecular orbital energy) is associated with the electron donating ability of a molecule, whereas the E_{LUMO} (the lowest unoccupied molecular orbital energy) characterizes the electron receiving tendency of a molecule. It can be seen from Fig. 15 that HOMO is spread principally on the aniline and N8 atom, while the population of LUMO is mainly distributed on the one pyridine ring and N8 atom. Thus, N8 atom is the main adsorption center and one pyridine ring acts as the main sites to accept electrons from the iron atoms with its anti-bonding orbital to form a feedback bond. Also the aniline part behaves as the dominant site to donate electrons to the unoccupied *d*-orbital of the iron atom to form

coordinate bonds.[4, 18] It is evident from Table 4 that APMA has a high E_{HOMO}, indicating that APMA has a tendency to adsorb on the mild steel surface. A molecule with small value of ΔE is easily polarized, resulting in easily adsorbing of APMA onto the metal surface.[45] The increase of the dipole moment (μ) probably increases the inhibition efficiency, which could be related to the dipole - dipole interaction of the molecules and the metal surface.[46] The values of μ follow the order: APMA > H_2O (1.85 D), indicating that APMA can adsorb on the mild steel by displacing H_2O molecules, thereby inhibiting the mild steel against corrosion.

Table 4 Quantum chemical parameters of APMA

inhibitor	E_{HOMO} (eV)	E_{LUMO} (eV)	ΔE (eV)	μ (D)	ΔN_{100}	ΔN_{110}	ΔN_{111}
APMA	-4.096	-1.382	2.714	2.94	0.43	0.77	0.42

The quantities of ionization potential (I) and electron affinity (A) are defined as $I = - E_{HOMO}$ and $A = - E_{LUMO}$, respectively.[22] Then the absolute electronegativity (χ) and global hardness (γ) are approximated as follows:[47]

$$\chi = (I + A) / 2 \quad (14)$$

$$\gamma = (I - A) / 2 \quad (15)$$

A perusal of literature[4, 48, 49] reveals that the work function (Φ) of the metal surface is an appropriate measure of its electronegativity and the fraction of electron (ΔN) transferred from the inhibitor to iron can be calculated as follows:

$$\Delta N = (\Phi - \chi_{inh}) / [2(\gamma_{Fe} + \gamma_{inh})] \quad (16)$$

where $\gamma_{Fe} \approx 0$ eV, Φ values obtained from DFT calculation are 3.88 eV, 4.82 eV, and 3.91 eV for Fe (1 1 1), (1 1 0), (1 0 0) planes, respectively.[22, 48] Accordingly, if $\Delta N < 0$, the electrons transfer from the metal to the inhibitor and vice versa if $\Delta N > 0$. In this study, all the values of ΔN are positive, indicating that APMA is an electron donator, favoring the formation of adsorption film on metal surface.

3.8. Molecular dynamics simulations

In order to better understand the adsorption behavior of APMA on the mild steel surface, the MD simulations were carried out. The system reaches equilibrium only if both of the energy and temperature reach balance.[17, 18, 22] As can be seen from Fig. 16, one pyridine ring adsorbs nearly parallel to the Fe (1 1 0) surface, while the rest two aromatic rings adsorb onto the Fe (1 1 0) surface in apparent tilted orientation. Therefore, the non-planar adsorption of APMA indicates that the steric effect plays an important role in the adsorption mode.

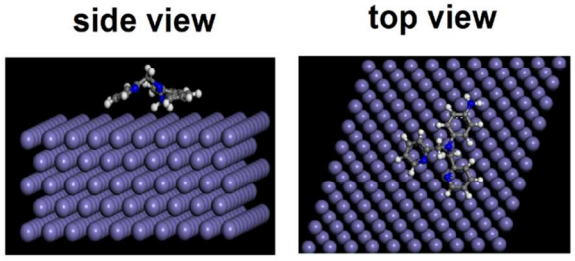

Fig. 16. Equilibrium adsorption configurations performed for APMA on Fe (1 1 0) surface

The values of both interaction energy and binding energy of APMA are given in Table 5. The negative value of E_{int} indicates attractive interactions.

Table 5 Interaction and binding energies between the inhibitor molecules and Fe (1 1 0) surface

Systems	E_{int} (kJ mol^{-1})	E_{bin} (kJ mol^{-1})
Fe + APMA	-603.0	603.0

3.9. Mechanism of corrosion inhibition

Generally, the adsorption process depends on many factors, including the nature of the metal, electronic structure, molecular size and chemical properties of the inhibitor.[29] Based on the results obtained from the experimental and theoretical analysis, a credible inference of the corrosion inhibition mechanism can be proposed. It is well known that the metal has an affinity towards heterocycles and abundance π electrons. Hence, APMA may adsorb on the mild steel surface via the chemisorption on the basis of donor-acceptor interactions between the vacant *d*-orbital of the iron atoms and the lone pair electrons on the N atoms as well as π electrons in the atomatic rings. N8 atom is the main adsorption center and one pyridine ring acts as the main sites to accept electrons from the iron atoms with its anti-bonding orbital to form a feedback bond. Meanwhile, the aniline part behaves as the dominant site to donate electrons to the unoccupied *d*-orbital of the iron atom to form coordinate bonds. Some researchers have reported that mild steel surface carries positive excess charge in the acidic solution,[17-19, 50] and APMA molecules should be protonated in hydrochloric acid solution. The protonated APMA molecules can hardly approach the metal surface because of the electrostatic repulsion. Thus the hydrated chloride ions are specifically adsorbed onto the mild steel surface to create an excess negative charge at first, favoring the adsorption of protonated APMA. Above all, the adsorption of APMA onto the mild steel surface includes both physisorption and chemisorption.

4. Conclusions

In summary, 4-amino-N, N-di-(2-pyridylmethyl)-aniline (APMA) was synthesized and evaluated as a corrosion inhibitor for mild steel in 1.0 M HCl. The experimental results showed that APMA was a mixed type inhibitor, retarding both anodic metal dissolution and cathodic hydrogen evolution reactions. The EIS results specified that dissolution of mild steel was prevented by the adsorption of APMA on the metal surface. The adsorption behavior obeyed Langmuir adsorption isotherm. Quantum chemical calculations showed that N8 atom is the main adsorption center and one pyridine ring acts as the main sites to accept electrons from the iron atoms with its anti-bonding orbital to form a feedback bond. Meanwhile, the aniline part behaves as the dominant site to donate electrons to the unoccupied *d*-orbital of the iron atom to form coordinate bonds. The molecular dynamics simulations results revealed that the non-planar adsorption of APMA molecules on the Fe (110) surface. The surface analysis experiments (SEM-EDX, XPS) confirmed the adsorption of APMA on the mild steel surface.

Acknowledgements

Financial supports from the National Major Science and Technology Program for Water Pollution Control and Treatment (2013ZX07210 - 001) are highly appreciated.

Notes and references

[a] Department of Applied Chemistry, School of Science, Nanjing Tech University, Nanjing 210009, China. E-mail: yangwznjtech@163.com. Tel: +86 25 83172359

[b] School of Environmental and Safety Engineering, Jiangsu Polytechnic University, Changzhou 213164, China

† Electronic Supplementary Information (ESI) available: ^{1}H, ^{13}C NMR, MS and FTIR spectra of 4-amino-N, N-di-(2-pyridylmethyl)-aniline. See DOI: 10.1039/b000000x/

1 X. H. Li, S. D. Deng, H. Fu and T. H. Li, *Electrochim. Acta*, 2009, **77**, 4089.
2 E. Bayol, T. Gürten, A. A. Gürten and M. Erbil, *Mater. Chem. Phys.*, 2008, **112**, 62.
3 H. Keleş, M. Keleş, İ. Dehri and O. Serindağ, *Mater. Chem. Phys.*, 2008, **112**, 173.
4 S. Kumar, D. Sharma, P. Yadav and M. Yadav, *Ind. Eng. Chem. Res.*, 2013, **52**, 14019.
5 J. J. Fu, H. S. Zang, Y. Wang, S. N. Li, T. Chen and X. D. Liu, *Ind. Eng. Chem. Res.*, 2012, **51**, 6377.
6 J. J. Fu, S. N. Li, Y. Wang, X. D. Liu and L. D. Lu, *J. Mater. Sci.*, 2011, **46**, 3550.
7 N. A. Negm, F. M. Ghuiba and S. M. Tawfik, *Corros. Sci.*, 2011, **53**, 3566.
8 A. K. Singh, *Ind. Eng. Chem. Res.*, 2012, **51**, 3215.
9 H. Gerengi and H. I. Sahin, *Ind. Eng. Chem. Res.*, 2012, **51**, 780.
10 Sudheer and M. A. Quraishi, *Ind. Eng. Chem. Res.*, 2014, **53**, 2851.
11 Y. M. Tang, X. Y. Yang, W. Z. Yang, R. Wan, Y. Z. Chen and X. S. Yin, *Corros. Sci.*, 2010, **52**, 1801.
12 A. Kosari, M. H. Moayed, A. Davoodi, R. Parvizi, M. Momeni, H. Eshghi and H. Moradi, *Corros. Sci.*, 2014, **78**, 138.
13 R. Yıldız, A. Döner, T. Doğan and İ. Dehri, *Corros. Sci.*, 2014, **82**, 125.
14 B. D. Mert, A. O. Yüce, G. Kardas and B. Yazıcı, *Corros. Sci.*, 2014, **85**, 287.
15 F. Zhang, Y. M. Tang, Z. Y. Cao, W. H. Jing, Z. L. Wu and Y. Z. Chen, *Corros. Sci.*, 2012, **61**, 1.
16 I. B. Obot and Z. M. Gasem, *Corros. Sci.*, 2014, **83**, 359.
17 B. Xu, W. Z. Yang, Y. Liu, X. S. Yin, W. N. Gong and Y. Z. Chen, *Corros. Sci.*, 2014, **78**, 260.
18 B. Xu, W. N. Gong, K. G. Zhang, W. Z. Yang, Y. Liu, X. S. Yin, H. Shi and Y. Z. Chen, *J. Taiwan. Inst. Chem. E.*, 2015, **51**, 193.
19 B. Xu, Y. Liu, X. S. Yin, W. Z. Yang and Y. Z. Chen, *Corros. Sci.*, 2013, **74**, 206.
20 K.F. Khaled and M. A. Amin, *Corros. Sci.*, 2009, **51**, 2098.
21 S. Lindsay, S. K. Lo, O. R. Maguire, E. Bill, M. R. Probert, S. Sproules and C. R. Hess, *Inorg. Chem.*, 2013, **52**, 898.
22 Z. Y. Cao, Y. M. Tang, H. Cang, J. Q. Xu, G. Lu and W. H. Jing, *Corros. Sci.*, 2014, **83**, 292.
23 S. D. Deng, X. H. Li and X. G. Xie, *Corros. Sci.*, 2014, **80**, 276.
24 S. Shahabi, P. Norouzi and M. R. Ganjali, *RSC Adv.*, 2015, **5**, 20838.
25 G. M. Abu El-Reash, O.A. El-Gammal and A. H. Radwan, *Spectrochim. Acta, Part A*, 2014, **121**, 259.
26 Y. M. Tang, F. Zhang, S. X. Hu, Z. Y. Cao, Z. L. Wu and W. H. Jing, *Corros. Sci.*, 2013, **74**, 271.
27 F. Mansfeld, *Corros. Sci.*, 2005, **47**, 3178.
28 E. McCafferty, *Corros. Sci.* 2005, **47**, 3202.
29 D. M. Gurudatt and K. N. Mohana, *Ind. Eng. Chem. Res.*, 2014, **53**, 2092.
30 E. S. Ferreira, C. Giancomelli, F. C. Giacomelli and A. Spinelli, *Mater. Chem. Phys.*, 2004, **83**, 129.
31 W. H. Li, Q. He, S. T. Zhang, C. L. Pei and B. R. Hou, *J. Appl. Electrochem.*, 2008, **38**, 289.
32 C. Cao, *Corros. Sci.*, 1996, **38**, 2073.
33 A. Y. Musa, A. A. H. Kadhum, A. B. Mohamad and M. S. Takriff, *Corros. Sci.*, 2010, **52**, 3331.
34 K. Shimizu, A. Lasia and J.-F. Boily, *Langmuir*, 2012, **28**, 7914.
35 X. H. Li, S. D. Deng and H. Fu, *Corros. Sci.*, 2011, **53**, 302.
36 X. W. Zheng, S. T. Zhang, M. Gong and W. P. Li, *Ind. Eng. Chem. Res.*, 2014, **53**, 16349.
37 M. A. Chidiebere, E. E. Oguzie, L. Liu, Y. Li and F. Wang, *Ind. Eng. Chem. Res.*, 2014, **53**, 7670.
38 G. N. Mu, X. H. Li, Q. Qu and J. Zhou, *Corros. Sci.*, 2006, **48**, 445.
39 A. O. Yüce and G. Kardas, *Corros. Sci.*, 2012, **58**, 86.
40 T. B. Gu, Z. J. Chen, X. H. Jiang, L. M. Zhou, Y. W. Liao, M. Duan, H. Wang and Q. Pu, *Corros. Sci.*, 2015, **90**, 118.
41 A. Adewuyi, A. Göpfert and T. Wolff, *Ind. Crops Prod.*, 2014, **52**, 439.
42 H. Zarrok, A. Zarrouk, B. Hammouti, R. Salghi, C. Jama and F. Bentiss, *Corros. Sci.*, 2012, **64**, 243.
43 F. Bentiss, C. Jama, B. Mernari, H. E. Attari, L. E. Kadi, M. Lebrini, M. Traisnel and M. Lagrenée, *Corros. Sci.*, 2009, **51**, 1628.
44 V. S. Sastri, M. Elboujdaini, J. R. Romn and J. R. Perumareddi, *Corros*., 1996, **52**, 447.
45 L. C. Murulana, M. M. Kabanda and E. E. Ebenso, *RSC Adv.*, 2015, **5**, 28743.
46 B. D. Mert, M. E. Mert, G. Kardaş and B. Yazıcı, *Corros. Sci.*, 2011, **53**, 4265.
47 R. G. Pearson, *J. Am. Chem. Soc.*, 1985, **107**, 6801.
48 A. Kokalj, *Electrochim. Acta*, 2010, **56**, 745.
49 A. Kokalj, *Chem. Phys.*, 2012, **393**, 1.
50 K. G. Zhang, B. Xu, W. Z. Yang, X. S. Yin, Y. Liu and Y. Z. Chen, *Corros. Sci.*, 2015, **90**, 284.